Original Research Article

Predicting Hidden Anatomical Target Patterns from Bioelectric Changes during Simulated Tissue Regeneration

Vivaan Patni

Deira International School, Al Badia Boulevard, Dubai Festival City, P.O. Box 79043, Dubai, United Arab Emirates

ABSTRACT

Bioelectric signals help cells coordinate tissue shape during development and regeneration, but it is unclear whether a hidden pattern can be inferred from voltage correction after damage. This study tested whether a partial simulated voltage movie could reconstruct a hidden target-voltage map and predict one of two regenerative outcome classes. A two-dimensional tissue model contained 508 active positions, and 160 independent baseline trajectories were evaluated across six observation windows and five levels of measurement noise. At 5% noise and 30% observation, inverse-movie accuracy was 95.6% (95% confidence interval [CI], 91.9%–98.8%), area under the receiver-operating-characteristic curve was 0.995, anatomical macro-Dice was 0.861, and normalised root-mean-square error was 0.145. Accuracy exceeded the immediate post-damage snapshot by 0.450 (95% CI, 0.362–0.537), but differed from the same-time snapshot by only 0.006 (95% CI, 0.000–0.019). A separate 160-trajectory holdout cohort with shifted parameter ranges reached 95.0% accuracy. All three declared misspecification conditions also reached 95.0% accuracy. When outcome targets were made partially overlapping and their separation was reduced to 0.15 of the original difference, accuracy fell to 62.5%. Ablations showed that smoothing and coefficient bounds materially affected spatial reconstruction, although binary accuracy was unchanged. Correction and coupling rates remained poorly identifiable despite accurate target prediction. These results support target reconstruction within this declared simulation, but they do not establish recovery of the biological mechanism or a universal voltage-to-anatomy code.

Keywords: Bioelectricity; regeneration; inverse modelling; target pattern; bistability; dynamical systems

INTRODUCTION

Regeneration requires individual cells to act together to restore an overall body pattern. In this study, the bioelectric state refers to spatial and temporal patterns of resting membrane potential generated by ion channels, pumps, and gap-junctional coupling. Researchers have proposed that these signals help coordinate growth and repair (1–3). Voltage changes can affect gene expression, cell division, cell movement, and tissue patterning, so they may guide cell behaviour instead of simply recording it (1–3).

Experiments in Xenopus frogs have linked regional voltage and pH patterns to facial development (4), membrane voltage to eye patterning (5), and resting-voltage gradients to neural development through Notch signalling (6). A transient sodium current has also been shown to initiate Xenopus tadpole tail regeneration (7). These studies support the idea that voltage can

Corresponding author: Vivaan Patni, E-mail: vivaanpatni2010@gmail.com.

Accepted August 17, 2026
https://doi.org/10.70251/HYJR2348.4412071219

help control biological patterns. However, they do not show that one universal voltage code describes every anatomical structure.

Planarians, which are small flatworms, provide clear examples of pattern control after injury. Voltage controlled by the H,K-ATPase pump is needed for normal head regeneration, while nerve signals and gap junctions help control long-range body polarity (8, 9). Blocking gap junctions can produce several possible head shapes, and short-term changes to natural voltage gradients can affect later rounds of regeneration (10, 11). Early bioelectric signals can influence anterior-posterior polarity (12). This connects planarian regeneration to anatomical homeostasis: the capacity of a living system to detect perturbation, regulate repair toward a stable morphology, and terminate growth after restoration (13).

One useful mathematical idea is bistability, which means that a system can settle into either of two stable states. Ion-channel models show that voltage-dependent feedback can support bistable resting-potential states (14). In bistable models, random changes or starting conditions near the boundary between states can lead similar tissues to different outcomes (15). The voltage immediately after injury may not reveal the final state, but the direction and speed of later voltage correction may provide more information.

Earlier computational studies have directly encoded possible target shapes (16), worked backward from altered shapes to infer regulatory networks (17), and described regeneration as error correction toward an anatomical set point (18). These studies suggest an inverse problem. Instead of giving a model a target and simulating repair, could the target be estimated from the repair process itself?

Detailed simulators can model spatial bioelectric signalling (19), and closed-loop models can describe how tissues work toward a target shape (20). This study focused on a narrower computational question: whether a hidden target-voltage map could be reconstructed from part of a noisy voltage movie and compared fairly with snapshots taken immediately after damage and at the same later time.

The study asked whether an inverse model could use voltage changes after simulated damage to reconstruct the hidden target-voltage map and predict the anatomical outcome class toward which the tissue was moving.

The primary hypothesis was that, at the declared main benchmark of 5% measurement noise and 30% movie observation, the inverse movie would predict the final original or alternate outcome class more accurately than the immediate post-damage snapshot. The corresponding primary endpoint was the paired difference in binary outcome accuracy. Comparisons with the same-time snapshot, longer observation, measurement noise, target-map reconstruction, and the additional validation analyses were secondary or exploratory. Because voltage is not known to have a universal one-to-one relationship with anatomy, the study continued to separate reconstruction of a target-voltage map from translation of that map into an anatomical pattern with a fixed codebook.

METHODS AND MATERIALS

Study Design

This was an in silico proof-of-concept study. A forward model created voltage trajectories for damaged tissue with a known hidden target-voltage map. A separate inverse calculation received only noisy voltage observations and attempted to reconstruct that map. One independently generated trajectory was the unit of analysis. The 160-trajectory baseline cohort defined the main analysis, and all additional stress tests were treated as exploratory validation. The study used no human participants, animals, patient records, or biological samples.

Tissue Geometry and Target Codebook

The simulated tissue was an ellipse placed on a 22 × 44 rectangular grid. Of 968 possible grid positions, 508 were inside the tissue mask. Each active position was a dimensionless tissue element, not a literal biological cell. The original target-voltage map had an anterior region on the left, a neutral trunk, and a posterior region on the right. The alternate map had anterior identity at both ends. Eighteen nearest-neighbour diffusion passes with weight 0.20 smoothed the sharp boundaries so that target voltage changed gradually between regions.

A fixed codebook connected normalised voltage to anatomical identity: −1 represented posterior tissue, 0 represented trunk tissue, and +1 represented anterior tissue. Each reconstructed value was assigned to the closest of these three values. These dimensionless values did not represent millivolts. The decoder was fixed before performance was measured. The study therefore tested anatomical-pattern prediction using a supplied codebook; it did not discover a biological voltage code.

Target-Separation Stress Test

The original target-voltage maps were separated by a fixed continuous difference. Their Euclidean distance,

root-mean-square difference, normalised root-mean-square difference, mean absolute difference, decoded-label disagreement, and decoded macro-Dice were calculated across the 508 active positions. A separate matched cohort used seed 20460721 to reduce the difference between outcome targets to scales of 1.00, 0.65, 0.35, and 0.15. For the three reduced-separation conditions, a trajectory-specific target offset ε was sampled from a normal distribution with mean 0 and standard deviation 0.18. The offset was fixed within that trajectory, which made the two outcome-class target distributions overlap. The target selector was limited to 0–1, while the inverse method and decision threshold were unchanged.

Damage and Hidden Target Selection

Each baseline trajectory began at the original target-voltage map. A posterior strip with a requested size sampled uniformly from 18%–55% of active positions was reset with independent values from $N(0, 0.12^2)$. Independent starting noise from $N(0, 0.025^2)$ was then added across the tissue. A hidden memory state, q, selected the target. Values near 0 favoured the original map U_0, while values near 1 favoured the alternate map U_1. The starting value q_0 was placed on either side of the unstable boundary $q = 0.5$ at a log-uniform distance from 0.005 to 0.35, conditional on a balanced initial side. Requested damage fraction, base k, D, r, σq, σV, and CV were sampled independently. Realised damage was the discretised grid fraction produced by the requested value, and k_i was conditionally generated from base k and CV.

At each time point, the current target-voltage map was

$$U(q) = (1 - q)U_0 + qU_1. \quad \text{(Eq. 1)}$$

The stochastic bistable memory followed

$$dq = r\,q(1 - q)(q - 0.5)dt + \sigma q\,q(1 - q)dWq. \quad \text{(Eq. 2)}$$

In Eq. 2, r was the memory rate, σq was the memory-noise amplitude, and dWq was a Gaussian Wiener increment. The $q(1 - q)$ multiplier reduced random movement near the endpoints, and q was limited to 0–1 after each step. A baseline trajectory was labelled original when final q was below 0.5 and alternate when it was at or above 0.5. The corresponding pure endpoint map, U_0 or U_1, was the correct baseline reconstruction target. The target-overlap stress tests instead used the declared trajectory-specific mixed target.

Forward Bioelectric Dynamics

The voltage V at active position i followed a correction-and-coupling equation:

$$dV_i = [k_i(U_i(q) - V_i) + D\,L(V)_i]dt + \sigma V\,dW_i. \quad \text{(Eq. 3)}$$

In Eq. 3, k_i was the correction rate at position i, D controlled nearest-neighbour coupling, $L(V)_i$ was the degree-normalised four-neighbour graph Laplacian, σV was the voltage-process noise amplitude, and dW_i was an independent Gaussian Wiener increment. Edges connected only active nearest neighbours, with no coupling to positions outside the tissue mask. For each trajectory, a base k and coefficient of variation (CV) were sampled independently. The spatial field was then sampled as $k_i = k[1 + N(0, CV^2)]$, limited to 0.25k–2k, and held fixed over time. Euler–Maruyama integration used $dt = 0.05$ for 220 steps, giving $T = 11$ normalised time units. Voltage was limited to −1.5 to +1.5 for numerical stability. Table 1 gives all fixed values, distributions, and limits. Figure 1 summarises the model.

Cohort and Observation Conditions

A fixed pseudorandom seed (20260718) generated 160 independent baseline trajectories. Each forward trajectory and its parameter set were reused across all five measurement-noise levels and six observation windows, which preserved paired comparisons without creating extra independent samples. A new Gaussian measurement-noise realisation was generated for each σm level and then reused across the observation windows at that level. The inverse method received the first 5%, 10%, 15%, 20%, 30%, or 50% of each movie.

Holdout and Model-Misspecification Tests

An independent holdout cohort of 160 trajectories used seed 20360721 and shifted ranges: $|q_0 - 0.5|$ was log-uniform from 0.004–0.30; f was 0.22–0.60; k was 0.50–1.25; D was 0.04–0.28; r was 1.3–3.2; σq was 0.12–0.34; σV was 0.004–0.014; and CV was 0.10–0.26. The same holdout settings were used for three deliberate forward-model misspecifications: nonlinear correction $k_i \tanh[U - V]$, a time-varying rate $k_i[1 + 0.35 \sin(2\pi t/T)]$, and anisotropic coupling with horizontal and vertical weights of 1.5 and 0.5. The inverse equation, coefficient limits, codebook, $\hat{q} = 0.5$ classification threshold, and 5% noise with 30% observation benchmark were not retuned.

Table 1. *Dimensionless forward-model and inverse-reconstruction design for the baseline cohort of 160 trajectories. H×W is grid height by width; dt is the integration step; T is total simulated time; q_0 is the initial hidden memory state; CV is the coefficient of variation of the spatial correction-rate field; D is electrical coupling; σq is memory-noise amplitude; σV is voltage-process noise amplitude; and σm is measurement-noise standard deviation. Uniform and log-uniform distributions were sampled independently unless a dependency is stated. These values are dimensionless simulation parameters, not biological measurements.*

Component	Symbol	Distribution or value	Role or limit
Tissue	H×W	22×44; 508 active	Fixed ellipse and spatial lattice
Target smoothing	–	18 passes; weight 0.20	Fixed transition smoothing
Time	dt, T	0.05; 11.0	220 Euler–Maruyama steps
Damage fraction	f	Uniform(0.18, 0.55)	Requested posterior fraction reset
Damage reset	–	$N(0, 0.12^2)$	Values within damaged strip
Initial field noise	–	$N(0, 0.025^2)$	Independent active-position noise
Initial memory distance	$\|q_0-0.5\|$	Log-uniform(0.005, 0.35)	Starting side balanced
Correction rate	k	Uniform(0.60, 1.15)	Base attraction toward target
Correction heterogeneity	CV	Uniform(0.08, 0.22)	Sets fixed k_i field; limited to 0.25k–2k
Electrical coupling	D	Uniform(0.06, 0.24)	Nearest-neighbour voltage coupling
Memory rate	r	Uniform(1.5, 3.0)	Bistable q dynamics
Memory noise	σq	Uniform(0.15, 0.30)	Stochastic q movement
Process noise	σV	Uniform(0.003, 0.012)	Voltage-process variation
Measurement noise	σm	0, 0.02, 0.05, 0.10, 0.15	Independent observation error
State limits	q, V	0–1; −1.5–1.5	Applied after each simulation step
Inverse bounds	$\hat{k}$, $\hat{D}$	0.08–2.0; 0–0.60	Applied after least-squares fitting

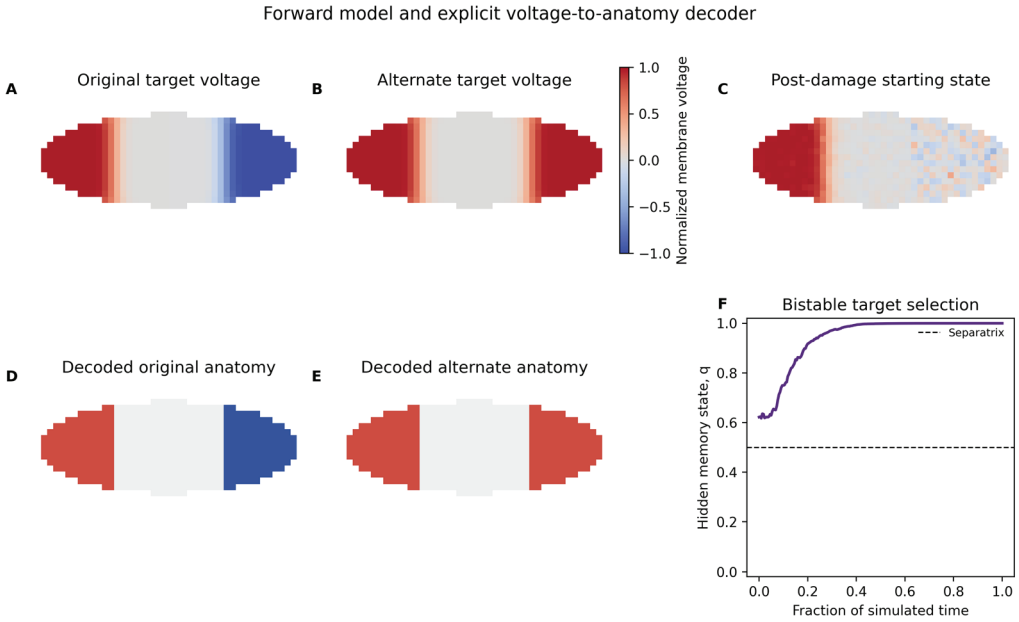

Figure 1. *Forward model and fixed decoder. The original and alternate target-voltage maps were translated into original or alternate anatomical patterns with a fixed three-level codebook. Damage reset a posterior strip, and hidden state q selected the outcome class. Colours show normalised voltage, not measured millivolts.*

Inverse Reconstruction from a Voltage Movie

The inverse method used a general system-identification idea: changes across a time series can provide clues about the equation that produced them (21). Voltage was smoothed and its time derivative was estimated with a second-order Savitzky–Golay filter (22). The largest valid odd window up to 21 frames was used. Writing Eq. 3 as $dV/dt = kU - kV + DL(V)$, the inverse approximation treated U as constant within each observation window so that each position's temporal mean could remove the unknown kU intercept. The forward U(q) remained time-varying and k_i remained spatially heterogeneous, so this was an explicit simplifying mismatch rather than an exact equality. Least-squares regression then estimated one global k and D from the centred variables:

$$(dV/dt)^c = k(-V^c) + D\,L(V)^c. \quad \text{(Eq. 4)}$$

In Eq. 4, superscript c denotes subtraction of each active position's temporal mean. The raw least-squares estimates were retained for identifiability analysis, while fitted values used for reconstruction were limited to $\hat{k}$ = 0.08–2.0 and $\hat{D}$ = 0–0.60. At each usable frame, the target-voltage map was estimated by rearranging Eq. 3:

$$\hat{U} = [(dV/dt) - \hat{D}\,L(V) + \hat{k}\,V] / \hat{k}\,. \quad \text{(Eq. 5)}$$

The temporal median of $\hat{U}$ at each position formed the reconstructed target-voltage map, which was limited to −1.5–1.5. No spatial regularisation was applied. An outcome score, $\hat{q}$, was calculated by projecting this map onto the line from U_0 to U_1. Scores at or above 0.5 predicted the alternate outcome class. $\hat{q}$ was an uncalibrated geometric score and was not interpreted as a probability. The same reconstructed map was separately translated into anterior, trunk, and posterior labels with the fixed nearest-value codebook.

Reconstruction Ablations and Identifiability

Paired ablations at the main benchmark removed Savitzky–Golay smoothing and used a numerical gradient, replaced the default derivative window of 21 with windows of 11 or 31, widened the coefficient limits to $\hat{k}$ = 0.01–4.0 and $\hat{D}$ = 0–1.20, or replaced the temporal median with a mean. All other settings were unchanged. Because the method used no spatial regularisation, there was no spatial penalty to ablate. A simulation-based parameter-recovery assessment compared $\hat{k}$ with both the sampled base k and the realised spatial mean of k_i, compared $\hat{D}$ with true D, retained raw estimates, counted coefficient-limit hits, measured correlations among true values, estimates, and signed errors, and examined prediction accuracy in large-error and boundary-hit subsets.

Snapshot Controls

Two snapshot controls were used. The immediate post-damage snapshot projected the first noisy frame onto the target line. This tested whether observed correction added information beyond the starting damage. The stricter same-time snapshot used the final noisy frame available in each observation window, so it contained the same elapsed repair time as the inverse movie. That frame was used for binary outcome prediction and was decoded as a target-voltage map for NRMSE and anatomical macro-Dice. The same-time snapshot separated information in the full movie from the simpler benefit of waiting longer.

Performance Measures

Accuracy measured the proportion of correctly predicted outcome classes. Area under the receiver-operating-characteristic curve (AUROC) measured separation across score thresholds. Target-voltage-map error was measured with normalised root-mean-square error (NRMSE), calculated by dividing root-mean-square error by the full prototype range of 2. Anatomical reconstruction was measured with pixel accuracy and macro-Dice, the unweighted mean Dice overlap across posterior, trunk, and anterior labels. When a label was absent from both the predicted and correct anatomical patterns, its Dice contribution was defined as 1.0. A case was called score-ambiguous when $|\hat{q} - 0.5| < 0.15$; performance after excluding these cases was reported with retained coverage. Final hidden states were also counted within the same margin of q = 0.5. The retrospective reliable-decision time was the first tested window at which a prediction was correct, $|\hat{q} - 0.5|$ was at least 0.15, and all later windows remained correct and confident. This rule used the known final outcome and later observations and was strictly exploratory. A separate prospective rule stopped at the second of two consecutive tested windows when the two predictions agreed and both scores were at least 0.15 from 0.5. It used only current and earlier observations, was fixed before holdout evaluation, and used final outcomes only to score decisions after stopping.

Software and Reproducibility

The simulation and analysis were written in Python 3.12 using NumPy (23), SciPy (24), Matplotlib (25), pandas (26), and scikit-learn (27). One self-contained source file generates the baseline analysis, holdout and challenge cohorts, ablations, trial-level outputs, summary files, and all figures with fixed seeds. No trained black-box model or external dataset was used.

Statistical Analysis

The main benchmark used 5% measurement noise and the first 30% of each movie. The primary endpoint was the paired difference in binary accuracy between the inverse movie and immediate post-damage snapshot for the 160 baseline trajectories. Accuracy, AUROC, macro-Dice, and NRMSE were summarised with 95% CIs from 2,000 trajectory-level bootstrap resamples. Paired differences used 4,000 paired trajectory resamples. An AUROC resample was redrawn if it contained only one outcome class.

The primary accuracy comparison used a two-sided exact McNemar test. Key secondary comparisons between the inverse movie and same-time snapshot were accuracy, macro-Dice, and NRMSE at the main benchmark. Accuracy used a two-sided exact McNemar test, continuous outcomes used two-sided Wilcoxon signed-rank tests, and the three P values were adjusted together with Holm's method. This hierarchy limited confirmatory testing to the primary endpoint and treated the adjusted same-time family as key secondary evidence. AUROC comparisons were exploratory. Their differences used 4,000 paired trajectory-bootstrap resamples and two-sided paired score-swap tests with 4,000 permutations. Observation-time, noise-grid, holdout, misspecification, target-difficulty, ablation, identifiability, ambiguity, and decision-time analyses were also exploratory. Full-grid movie-minus-same-time effects were reported for accuracy, AUROC, macro-Dice, and NRMSE across all 30 noise-window conditions, with Holm adjustment within each metric family. The paired unit was always the base trajectory.

RESULTS

Outcome Balance, Target Separation, and Ambiguity

Of the 160 baseline trajectories, 78 ended in the original outcome class and 82 ended in the alternate class. Final q was strongly concentrated near opposite endpoints. In the original class, the median was 0.000069, the IQR was 0.000004–0.000411, and the range was 0.00000001–0.099769. In the alternate class, the median was 0.999965, the IQR was 0.999600–0.999995, and the range was 0.831897–0.99999997. No trajectory ended within 0.15 of q = 0.5; the closest final state was 0.332 from the boundary. Thirty-four trajectories ended on the opposite side from their initial q_0, showing that stochastic memory dynamics could reverse the starting tendency. Figure 2 shows one alternate-class reconstruction example.

Across the 508 active positions, the two original

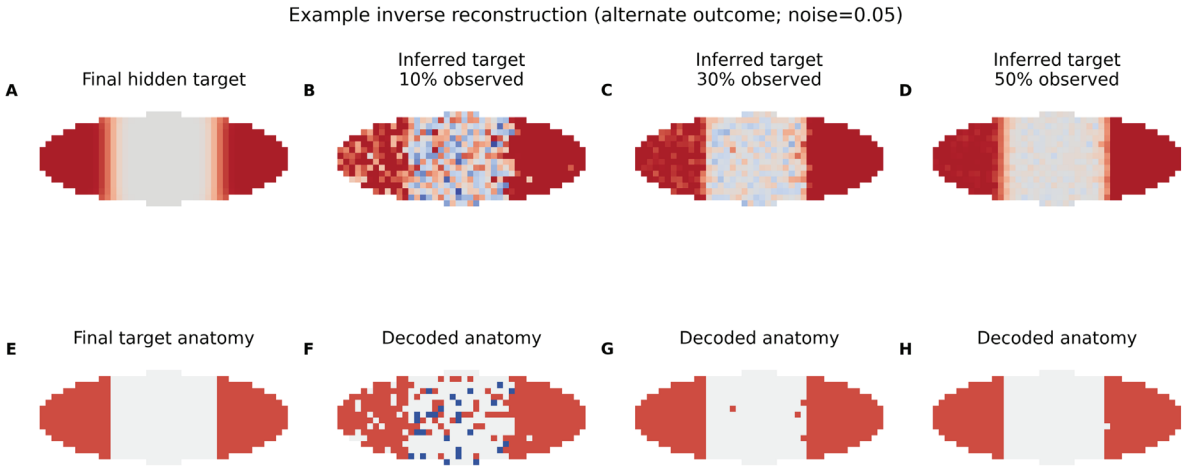

Figure 2. *Example inverse-movie reconstruction from one alternate-class baseline trajectory at 5% measurement noise. The top row compares the hidden final target-voltage map with reconstructions from the first 10%, 30%, and 50% of the movie. The bottom row shows the matching three-class anatomical patterns produced by the fixed decoder. Colours represent normalised voltage or anatomical identity. Results for all 160 trajectories are reported in the text, tables, and later figures.*

continuous target-voltage maps had Euclidean distance 21.103, root-mean-square difference 0.936, and NRMSE 0.468. Their decoded anatomical patterns differed at 24.0% of positions and had macro-Dice 0.556. At the main benchmark, 24 of 160 $\hat{q}$ scores were within 0.15 of the decision boundary. These cases had 70.8% accuracy and contained all seven errors. Excluding them retained 136 trajectories (85.0% coverage) with 100% accuracy. This exclusion analysis describes uncertainty in an uncalibrated projection score, not a predicted probability.

Primary Benchmark and Control Comparisons

At 5% measurement noise and 30% observation, inverse-movie accuracy was 0.956 (95% CI, 0.919–0.988) and AUROC was 0.995 (95% CI, 0.988–1.000). Mean anatomical macro-Dice was 0.861 (95% CI, 0.836–0.884), and mean target-voltage-map NRMSE was 0.145 (95% CI, 0.137–0.153) (Table 2).

The immediate post-damage snapshot reached 0.506 accuracy. The paired inverse-movie improvement was 0.450 (95% CI, 0.362–0.537). The inverse movie alone classified 77 trajectories correctly, while the immediate snapshot alone classified 5 trajectories correctly (two-sided exact McNemar $P = 1.20 \times 10^{-17}$). The primary hypothesis was therefore supported. The same-time snapshot reached 0.950 accuracy. Its paired difference from the inverse movie was only 0.006 (95% CI, 0.000–0.019; two-sided exact McNemar P = 1; Holm-adjusted P = 1). In the exploratory AUROC comparisons, the immediate snapshot reached 0.503, giving a movie-minus-snapshot difference of +0.492 (95% CI, 0.401–0.582; paired-permutation $P = 2.50 \times 10^{-4}$). The same-time snapshot reached 0.997, giving a difference of −0.001 (95% CI, −0.005–0.001; P = 0.511; 30-cell Holm-adjusted P = 1).

Inverse-movie macro-Dice was 0.046 higher than the same-time snapshot value (95% CI, 0.017–0.074; two-sided Wilcoxon P = 0.00163; Holm-adjusted P = 0.00488). Continuous NRMSE was 0.004 higher for the inverse movie (95% CI, −0.004–0.012; P = 0.69; Holm-adjusted P = 1). The movie improved decoded anatomical overlap at the main benchmark but did not improve continuous target-voltage-map error. A separate exploratory sensitivity analysis omitted labels that were absent from both compared maps. Under that definition, macro-Dice was 0.853 for the inverse movie and 0.784 for the same-time snapshot, a paired difference of 0.068 (95% CI, 0.040–0.096; two-sided Wilcoxon $P = 6.46 \times 10^{-6}$). The direction of the anatomical-overlap result was unchanged.

Prediction and reconstruction performance across all six observation windows at 5% measurement noise is shown in Figure 3. Binary accuracy generally increased with observation duration, while target-map NRMSE decreased.

Effect of Observation Time

At 5% measurement noise, target-voltage-map NRMSE was lower at 50% observation than at 10% observation. Mean NRMSE changed from 0.219 to

Table 2. *Primary benchmark and controls for the same 160 paired baseline trajectories at 5% measurement noise and 30% movie observation. The inverse movie uses all observed frames; the immediate post-damage snapshot uses the first frame; and the same-time snapshot uses the final frame available at 30% observation. CI is confidence interval; AUROC is area under the receiver-operating-characteristic curve; macro-Dice is the unweighted mean Dice overlap across the three anatomical labels, with an absent label scored as 1.0 when absent from both compared patterns; and NRMSE is normalised root-mean-square error over the full voltage range of 2. Values in parentheses are 95% bootstrap CIs. Accuracy P values use two-sided exact McNemar tests, AUROC P values use two-sided paired score-swap permutation tests, and macro-Dice and NRMSE P values use two-sided Wilcoxon signed-rank tests. The three key same-time comparisons of accuracy, macro-Dice, and NRMSE report Holm-adjusted P values; exploratory same-time AUROC reports Holm adjustment across its 30-condition grid.*

Measure	Inverse movie	Control	Paired comparison
Outcome accuracy	0.956 (0.919–0.988)	Immediate: 0.506	+0.450 (0.362–0.537); $P=1.20 \times 10^{-17}$
Outcome accuracy	0.956	Same-time: 0.950	+0.006 (0.000–0.019); P=1; Holm P=1
AUROC	0.995 (0.988–1.000)	Immediate: 0.503	+0.492 (0.401–0.582); $P=2.50 \times 10^{-4}$
AUROC	0.995	Same-time: 0.997	−0.001 (−0.005–0.001); P=0.511; grid Holm P=1
Anatomical macro-Dice	0.861 (0.836–0.884)	Same-time: 0.815	+0.046 (0.017–0.074); P=0.00163; Holm P=0.00488
Target NRMSE	0.145 (0.137–0.153)	Same-time: 0.141	+0.004 (−0.004–0.012); P=0.69; Holm P=1

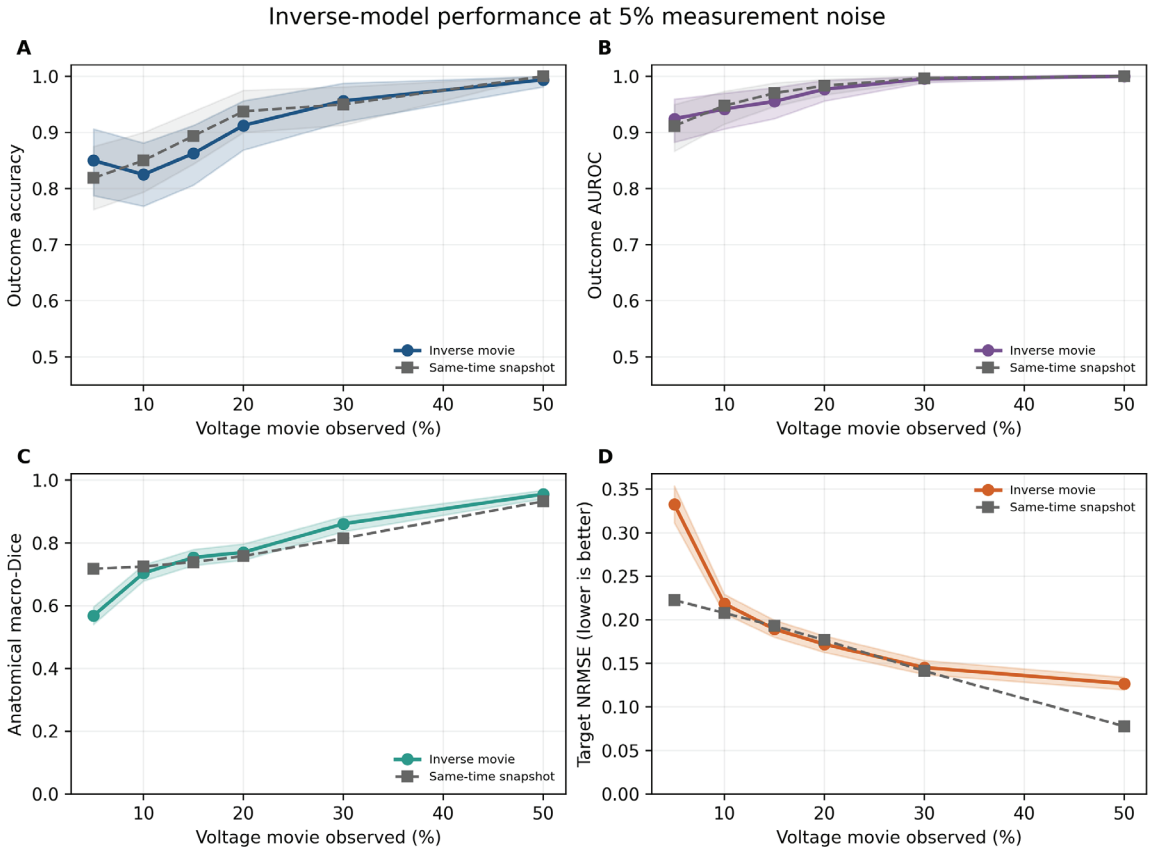

Figure 3. *Prediction and reconstruction performance across six observation windows at 5% measurement noise. Each point summarises the same 160 paired baseline trajectories. Accuracy is a proportion, AUROC is a cohort-level rank statistic, and macro-Dice and NRMSE are trajectory means. Shaded bands are 95% trajectory-bootstrap CIs from 2,000 resamples. Same-time snapshot curves use the last frame available at each window. AUROC is area under the receiver-operating-characteristic curve, and NRMSE is normalised root-mean-square error.*

0.127, a paired decrease of 0.092 (95% CI, 0.082–0.102; exploratory two-sided Wilcoxon P = 2.98 × 10^{-26}). Binary accuracy was 0.850 at 5% observation and 0.994 at 50%, while the same-time snapshot reached 1.000 at 50%.

Measurement Noise and Full Movie-Snapshot Grid

At 30% observation, baseline inverse-movie accuracy remained 0.956 across measurement-noise SDs from 0 to 0.15. Macro-Dice fell from 0.919 to 0.722, and NRMSE rose from 0.135 to 0.197. Across all 30 paired noise-window conditions, the inverse movie had higher, equal, and lower accuracy than the same-time snapshot in 7, 5, and 18 cells, respectively. AUROC was higher, tied, and lower in 2, 5, and 23 cells. Macro-Dice favoured the movie in 15 cells and the snapshot in 15; NRMSE favoured the movie in 11 and the snapshot in 19. The movie advantage was therefore condition- and metric-dependent. Table 3 reports the 30% noise series, Figure 4A–C shows accuracy, macro-Dice, and NRMSE point effects, and Supplementary Data File 1 (paired_movie_vs_snapshot_full_grid.csv) gives all four metrics for every condition, including paired effects, 95% CIs, raw two-sided P values, and Holm-adjusted P values.

Additional Validation Analyses

The independent shifted-range holdout reached 0.950 inverse-movie accuracy (95% CI, 0.912–0.981), macro-Dice 0.853, and NRMSE 0.148. All three declared misspecification conditions also reached 0.950 accuracy. The same-time snapshot reached 0.963 in the unmodified shifted holdout. In the target-difficulty series, inverse-movie binary accuracy changed from 0.956 at full separation to 0.625 when separation was 0.15 and class targets overlapped. For every reduced-separation

Table 3. *Measurement-noise robustness at 30% movie observation. Measurement-noise SD is the Gaussian measurement-error standard deviation on the normalised voltage scale. Each row summarises the same 160 paired baseline trajectories, so rows are repeated conditions rather than independent cohorts. The inverse movie uses all frames through 30% observation, and the same-time snapshot uses the final frame at that window. Macro-Dice is the unweighted mean Dice overlap across posterior, trunk, and anterior labels, with an absent label scored as 1.0 when absent from both compared patterns. NRMSE is normalised root-mean-square error over the full voltage range of 2. Reported values are trajectory means except accuracy, which is a proportion.*

Noise SD	Movie accuracy	Same-time accuracy	Movie macro-Dice	Same-time macro-Dice	Movie NRMSE
0.00	0.956	0.950	0.919	0.812	0.135
0.02	0.956	0.956	0.906	0.812	0.137
0.05	0.956	0.950	0.861	0.815	0.145
0.10	0.956	0.950	0.779	0.816	0.168
0.15	0.956	0.956	0.722	0.803	0.197

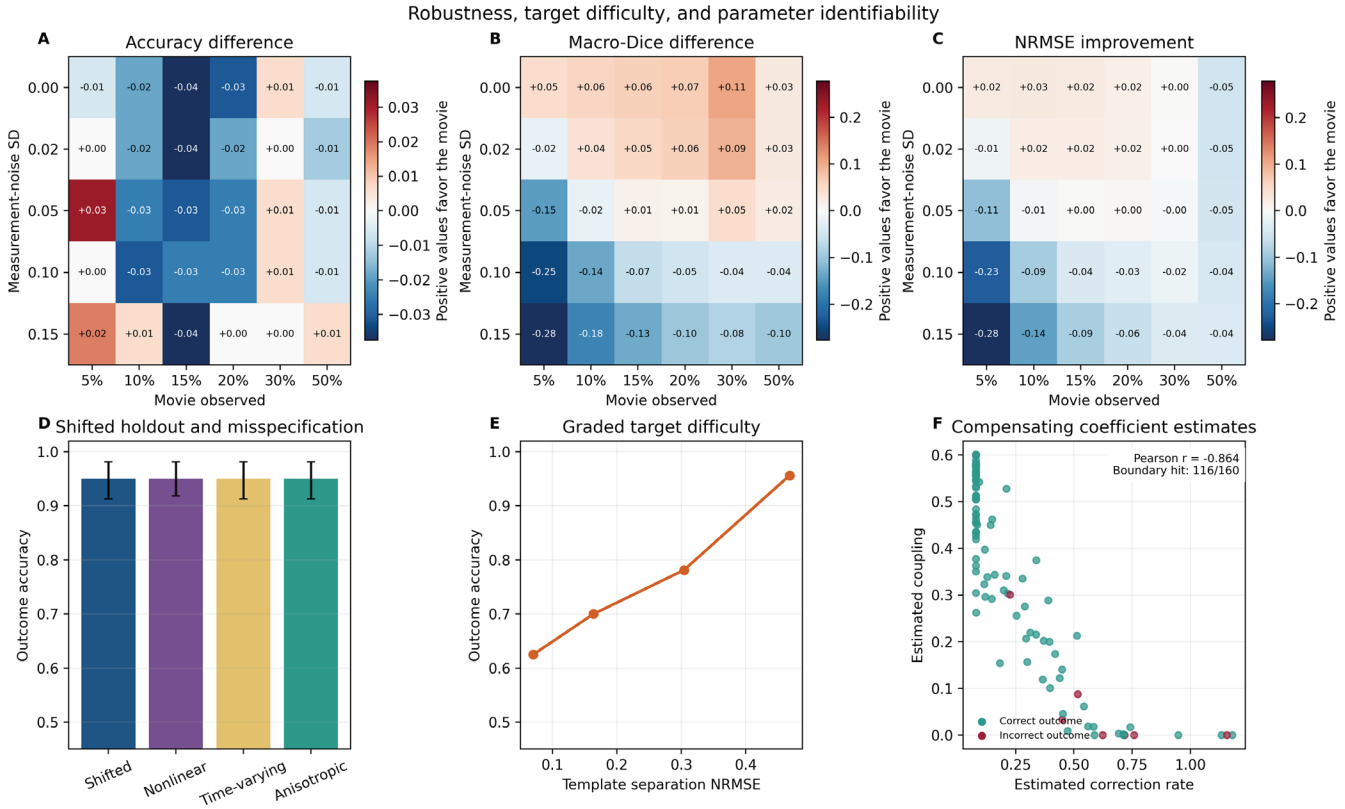

Figure 4. *Additional robustness, target-difficulty, and identifiability analyses. Panels A–C show paired inverse-movie versus same-time snapshot effects for all 30 combinations of six observation windows and five measurement-noise SDs in the same 160 baseline trajectories. Accuracy and macro-Dice are movie minus snapshot; NRMSE improvement is snapshot minus movie, so positive values favour the movie in every panel. Full-grid AUROC effects and all 95% CIs and adjusted P values are reported in Supplementary Data File 1. Panel D shows inverse-movie accuracy and 95% bootstrap CIs in the shifted-range holdout and three deliberately misspecified forward models, each with 160 trajectories at 5% noise and 30% observation. Panel E shows accuracy as target separation and class overlap changed in separate matched 160-trajectory cohorts. Panel F shows the compensating relation between estimated k and D at the baseline benchmark; teal points are correct predictions and red points are errors. NRMSE is normalised root-mean-square error, and SD is standard deviation on the normalised voltage scale.*

condition, smaller NRMSE partly reflected lower target amplitude. At separation scales 0.35 and 0.15, the fixed three-level decoder assigned both nominal targets the same anatomical labels, so macro-Dice was not outcome-discriminating in those two conditions. These stress tests supported partial generalisation but did not show a universal movie advantage.

Binary accuracy was 0.956 in every reconstruction ablation, but spatial reconstruction was sensitive to the pipeline. Default macro-Dice was 0.861 and NRMSE was 0.145. Without smoothing, macro-Dice was 0.570 and NRMSE was 0.316. Derivative windows of 11 and 31 produced macro-Dice values of 0.807 and 0.870, with NRMSE values of 0.154 and 0.144, respectively. Wider coefficient limits gave macro-Dice 0.605 and NRMSE 0.351; the temporal mean gave macro-Dice 0.870 and NRMSE 0.143. Smoothing and coefficient limits were therefore important for spatial estimates even when the widely separated baseline outcome classes remained easy to distinguish.

Parameter recovery indicated poor practical identifiability under the tested sampling and observation conditions. Sampled base k had median 0.854 (interquartile range [IQR], 0.697–1.017); the realised mean k_i was 0.859 (IQR, 0.694–1.021); and $\hat{k}$ was 0.080 (IQR, 0.080–0.202). True D had median 0.153 (IQR, 0.105–0.205), while $\hat{D}$ was 0.557 (IQR, 0.304–0.600). Pearson correlations were 0.181 for true versus estimated k and 0.029 for true versus estimated D. Estimated k and D were strongly negatively correlated ($r = -0.864$), as were their signed errors ($r = -0.747$), consistent with compensating parameter errors. The lower and upper k limits were hit in 107 and 0 trajectories, respectively; the lower and upper D limits were hit in 9 and 65. Overall, 116 of 160 (72.5%) hit at least one limit and had 96.6% prediction accuracy. Accuracy remained 98.6% among 138 trajectories with k relative error above 0.50 and 100% among 117 trajectories with D absolute error above 0.20. Accurate target prediction therefore did not identify the generating dynamics.

Exploratory Decision Timing

At 5% noise, the retrospective rule found a correct stable decision in 151 of 160 baseline trajectories, with a median earliest window of 10%; nine trajectories never met the rule. The no-decision counts at noise SDs 0, 0.02, 0.05, 0.10, and 0.15 were 9, 9, 9, 8, and 9. Under the prospective rule, 137 of 160 shifted-holdout trajectories produced a decision (85.6% coverage). Conditional accuracy was 97.1%, the median stopping window was 10.0% of the movie, and 23 trajectories did not stop by 50% observation. Figure 5 shows both analyses and includes non-decisions.

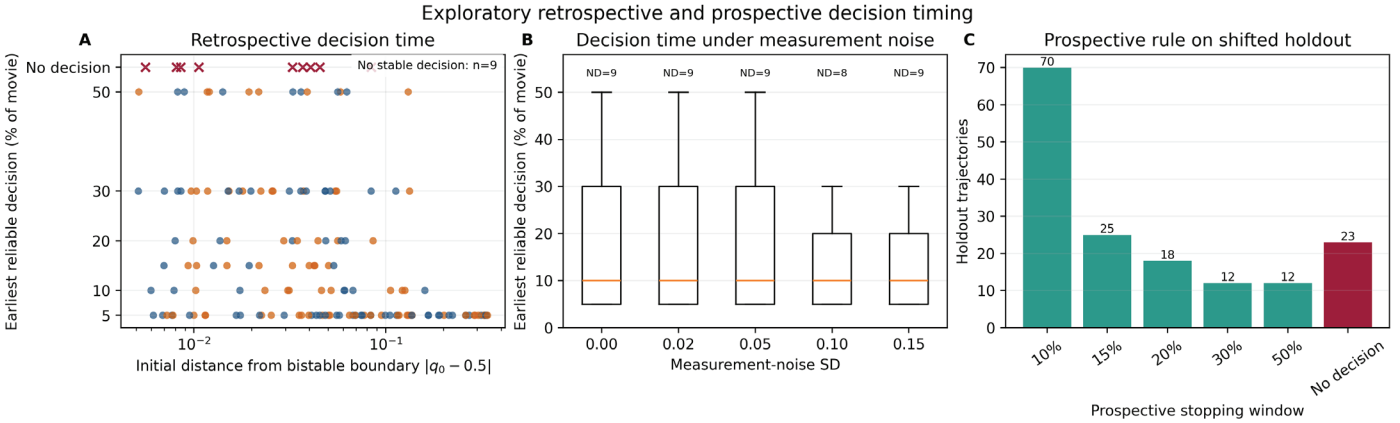

Figure 5. *Exploratory retrospective and prospective decision timing. Panel A shows the earliest retrospective reliable-decision window against the initial distance $|q_0-0.5|$ for the 160 baseline trajectories at 5% measurement-noise SD; crosses show the nine trajectories with no stable decision by 50% observation. Panel B summarises retrospective windows across all five noise SDs and labels each no-decision count. This retrospective rule used the final outcome and later windows and cannot be used prospectively. Panel C applies the fixed prospective rule to 160 shifted-range holdout trajectories: stopping occurred at the second of two consecutive agreeing predictions when both $|\hat{q}-0.5|$ values were at least 0.15. Bars show the stopping-window counts and the 23 trajectories with no decision.*

DISCUSSION

Main Finding

Within this declared simulation, a partial noisy voltage movie reconstructed a hidden target-voltage map and predicted which of two baseline outcome classes was selected. The original benchmark was reproduced exactly, and accuracy remained 0.950 in an independent shifted-range holdout and under the three tested misspecifications. The challenge series showed that binary outcome accuracy depended on target separation and class overlap. These findings are consistent with the broader idea that bioelectric states can help control biological patterns (1–3) and that regeneration may act as closed-loop error correction (18, 20). They do not show that a living tissue's complete anatomy can be read directly from voltage.

The analysis had three distinct steps. First, the inverse equation reconstructed a target-voltage map. Second, the supplied codebook translated voltage into an anatomical pattern. Third, the regression estimated correction and coupling coefficients. The first step was accurate in the baseline and retained useful performance in the declared stress tests. The second worked because the codebook was given. The third showed poor practical identifiability under the tested conditions. Weak true-estimated correlations, frequent coefficient-limit hits, and strong negative correlation between estimated k and D were consistent with compensating parameter errors that preserved target prediction without recovering the generating mechanism.

Why the Same-Time Control Changes the Conclusion

Comparison only with the immediate post-damage snapshot produced a large primary accuracy difference, but it mixed information from a movie with the effect of elapsed repair time. The same-time snapshot separated these effects. Across the 30 noise-window cells, inverse-movie accuracy was higher in only 7, tied in 5, and lower in 18. Macro-Dice and NRMSE also changed direction across conditions. At the main benchmark, the movie improved decoded anatomical overlap but not continuous target-voltage-map error. The value of the movie was therefore metric- and condition-dependent rather than universal.

Relation to Previous Work

Bistability was included because feedback between ion channels and voltage can support stable voltage memories (14). Random selection between pattern memories has also been proposed as one explanation for variable regeneration outcomes (15). The original and two-anterior targets were inspired by planarian studies in which bioelectric or gap-junction changes altered head-to-tail patterning (8–12). Even so, the grid, variables, and parameter values were abstract. They were not fitted to planarian voltage recordings, so the images should not be treated as a simulation of a particular species.

This work also differs from models that directly encode target shapes (16) or infer regulatory networks from many altered anatomical outcomes (17). Here, the input to the inverse method was a voltage time series after the same type of damage. Detailed bioelectric simulators such as the Bioelectric Tissue Simulation Engine (BETSE) include much richer models of ions, junctions, and tissue physics (19).

Strengths

The study had known correct target-voltage maps, nearly balanced baseline outcomes, paired controls, five noise levels, six observation windows, trajectory-level bootstrap intervals, exact paired tests, a fixed seed, and exact reproduction of the baseline benchmark. Additional analyses included an independent shifted-range holdout, three deliberate model misspecifications, partially overlapping target conditions, a full paired movie-snapshot grid, reconstruction ablations, a simulation-based identifiability assessment, and a genuinely prospective rule evaluated on held-out trajectories. Supported and unsupported results were reported separately.

Limitations

The inverse model still shared important structure with the forward model. The added misspecifications tested nonlinear correction, a time-varying correction rate, and anisotropic coupling, but not alternative boundary conditions, additional latent states, tissue growth, or a different voltage-to-anatomy codebook. The holdout changed parameter ranges but retained the same geometry and broad bistable mechanism, so it was an internal computational holdout rather than external validation.

The model used normalised voltage, time, and distance rather than biological units. It left out tissue growth, cell movement, mechanics, gene regulation, metabolism, and changes in tissue shape. The target-difficulty study used two outcome classes with overlapping target distributions; it did not test a multiclass anatomical code. At every reduced-separation scale, lower NRMSE partly followed from smaller target amplitude, and at scales 0.35 and 0.15 the fixed decoder mapped both nominal

targets to the same anatomical pattern. Excluding ambiguous $\hat{q}$ scores improved accuracy at the cost of 15% non-coverage, and $\hat{q}$ was not probability-calibrated. Confidence intervals describe variation within these simulations, not uncertainty in living tissues.

The original decision-time rule remained retrospective and exploratory. The prospective rule avoided later information but was tested only once on the shifted holdout and left 23 trajectories without a decision. Independent prospective replication is still needed. Poor recovery of k and D also shows that perturbations or independent measurements would be required to identify a biological mechanism.

Proposed Biological Validation

A future experiment could use live voltage reporters after a standard injury and score final anatomy without revealing the result to the prediction procedure. The voltage-to-anatomy decoder and prospective stopping rule should be fixed on separate samples. Gap-junction or ion-pump perturbations could shift regenerative states, based on earlier planarian experiments (8–12). A preregistered analysis should compare the inverse movie with immediate, same-time, time-shuffled, and constant-target controls, report non-decisions, and repeat the test across independent experimental batches.

CONCLUSION

A partial voltage-correction movie reconstructed the hidden target-voltage map and predicted an original or alternate baseline outcome with 95.6% accuracy in this simulation. The primary difference from the immediate post-damage snapshot was large, but same-time comparisons and the full condition grid showed no universal movie advantage. Binary outcome accuracy remained 95.0% in the shifted-range holdout and tested misspecifications, then declined under strongly overlapping targets. Smoothing and coefficient limits affected spatial reconstruction, and k and D were poorly identifiable despite accurate target prediction. The results therefore support a limited computational proof of concept when the correction framework and voltage-to-anatomy codebook are declared. They do not establish a universal biological decoder or recovery of the underlying mechanism.

FUNDING SOURCES

No external funding was received for this study.

CONFLICT OF INTEREST

The author declares that there are no conflicts of interest related to this work.

ETHICS STATEMENT

Not applicable. This computational study used no human participants, animals, identifiable records, or biological samples.

DATA AND CODE AVAILABILITY

The baseline source code and publication figures are available in the GitHub repository below. The additional single-file simulation, validation outputs, summary files, and regenerated figures accompany this submission and are intended to be archived in the same repository.

GitHub repository: https://github.com/vxxqv/Bioelectric-tissue-regeneration

REFERENCES

1. Levin M. Bioelectric signaling: Reprogrammable circuits underlying embryogenesis, regeneration, and cancer. *Cell*. 2021; 184 (8): 1971-1989. doi:10.1016/j.cell.2021.02.034.
2. Whited JL, Levin M. Bioelectrical controls of morphogenesis: from ancient mechanisms of cell coordination to biomedical opportunities. *Curr Opin Genet Dev*. 2019; 57: 61-69. doi:10.1016/j.gde.2019.06.014.
3. Levin M. Molecular bioelectricity: how endogenous voltage potentials control cell behavior and instruct pattern regulation in vivo. *Mol Biol Cell*. 2014; 25 (24): 3835-3850. doi:10.1091/mbc.E13-12-0708.
4. Vandenberg LN, Morrie RD, Adams DS. V-ATPase-dependent ectodermal voltage and pH regionalization are required for craniofacial morphogenesis. *Dev Dyn*. 2011; 240 (8): 1889-1904. doi:10.1002/dvdy.22685.
5. Pai VP, Aw S, Shomrat T, *et al*. Transmembrane voltage potential controls embryonic eye patterning in Xenopus laevis. *Development*. 2012; 139 (2): 313-323. doi:10.1242/dev.073759.
6. Pai VP, Lemire JM, Paré JF, *et al*. Endogenous gradients of resting potential instructively pattern embryonic neural tissue via Notch signaling and regulation of proliferation. *J Neurosci*. 2015; 35 (10): 4366-4385. doi:10.1523/JNEUROSCI.1877-14.2015.
7. Tseng AS, Beane WS, Lemire JM, *et al*. Induction of vertebrate regeneration by a transient sodium current.

J Neurosci. 2010; 30 (39): 13192-13200. doi:10.1523/JNEUROSCI.3315-10.2010.

8. Beane WS, Morokuma J, Lemire JM, *et al*. A chemical genetics approach reveals H,K-ATPase-mediated membrane voltage is required for planarian head regeneration. *Chem Biol*. 2011; 18 (1): 77-89. doi:10.1016/j.chembiol.2010.11.012.
9. Oviedo NJ, Morokuma J, Walentek P, *et al*. Long-range neural and gap junction protein-mediated cues control polarity during planarian regeneration. *Dev Biol*. 2010; 339 (1): 188-199. doi:10.1016/j.ydbio.2009.12.012.
10. Emmons-Bell M, Durant F, Hammelman J, *et al*. Gap junctional blockade stochastically induces different species-specific head anatomies in genetically wild-type Girardia dorotocephala flatworms. *Int J Mol Sci*. 2015; 16 (11): 27865-27896. doi:10.3390/ijms161126065.
11. Durant F, Morokuma J, Fields C, *et al*. Long-term, stochastic editing of regenerative anatomy via targeting endogenous bioelectric gradients. *Biophys J*. 2017; 112 (10): 2231-2243. doi:10.1016/j.bpj.2017.04.011.
12. Durant F, Bischof J, Fields C, *et al*. The role of early bioelectric signals in the regeneration of planarian anterior/posterior polarity. *Biophys J*. 2019; 116 (5): 948-961. doi:10.1016/j.bpj.2019.01.029.
13. Levin M, Pietak AM, Bischof J. Planarian regeneration as a model of anatomical homeostasis: recent progress in biophysical and computational approaches. *Semin Cell Dev Biol*. 2019; 87: 125-144. doi:10.1016/j.semcdb.2018.04.003.
14. Law R, Levin M. Bioelectric memory: modeling resting potential bistability in amphibian embryos and mammalian cells. *Theor Biol Med Model*. 2015; 12: 22. doi:10.1186/s12976-015-0019-9.
15. Pezzulo G, LaPalme J, Durant F, *et al*. Bistability of somatic pattern memories: stochastic outcomes in bioelectric circuits underlying regeneration. *Philos Trans R Soc Lond B Biol Sci*. 2021; 376 (1821): 20190765. doi:10.1098/rstb.2019.0765.
16. Lobo D, Solano M, Bubenik GA, *et al*. A linear-encoding model explains the variability of the target morphology in regeneration. *J R Soc Interface*. 2014; 11 (92): 20130918. doi:10.1098/rsif.2013.0918.
17. Lobo D, Levin M. Inferring regulatory networks from experimental morphological phenotypes: a computational method reverse-engineers planarian regeneration. *PLoS Comput Biol*. 2015; 11 (6): e1004295. doi:10.1371/journal.pcbi.1004295.
18. Pezzulo G, Levin M. Re-membering the body: applications of computational neuroscience to the top-down control of regeneration of limbs and other complex organs. *Integr Biol (Camb)*. 2015; 7 (12): 1487-1517. doi:10.1039/C5IB00221D.
19. Pietak AM, Levin M. Exploring instructive physiological signaling with the Bioelectric Tissue Simulation Engine. *Front Bioeng Biotechnol*. 2016; 4: 55. doi:10.3389/fbioe.2016.00055.
20. Grodstein J, McMillen P, Levin M. Closing the loop on morphogenesis: a mathematical model of morphogenesis by closed-loop reaction-diffusion. *Front Cell Dev Biol*. 2023; 11: 1087650. doi:10.3389/fcell.2023.1087650.
21. Brunton SL, Proctor JL, Kutz JN. Discovering governing equations from data by sparse identification of nonlinear dynamical systems. *Proc Natl Acad Sci U S A*. 2016; 113 (15): 3932-3937. doi:10.1073/pnas.1517384113.
22. Savitzky A, Golay MJE. Smoothing and differentiation of data by simplified least squares procedures. *Anal Chem*. 1964; 36 (8): 1627-1639. doi:10.1021/ac60214a047.
23. Harris CR, Millman KJ, van der Walt SJ, *et al*. Array programming with NumPy. *Nature*. 2020; 585 (7825): 357-362. doi:10.1038/s41586-020-2649-2.
24. Virtanen P, Gommers R, Oliphant TE, *et al*. SciPy 1.0: fundamental algorithms for scientific computing in Python. *Nat Methods*. 2020; 17 (3): 261-272. doi:10.1038/s41592-019-0686-2.
25. Hunter JD. Matplotlib: A 2D graphics environment. *Comput Sci Eng*. 2007; 9 (3): 90-95. doi:10.1109/MCSE.2007.55.
26. McKinney W. Data structures for statistical computing in Python. In: van der Walt S, Millman J, editors. Proceedings of the 9th Python in Science Conference. 2010: 56-61. doi:10.25080/Majora-92bf1922-00a.
27. Pedregosa F, Varoquaux G, Gramfort A, *et al*. Scikit-learn: machine learning in Python. *J Mach Learn Res*. 2011; 12: 2825-2830.